nature communications

Article

https://doi.org/10.1038/s41467-025-63388-0

Observation of triplet-assisted long-distance charge-transfer exciton transport in single organic cocrystal

Received: 13 March 2025

Accepted: 19 August 2025

Published online: 29 August 2025

Check for updates

Yejun Xiao[1], Xianchang Yan[1,2], Rui Cai[3], Xuan Liu[4], Jingwen Bao[1], Min Zhang[1,2], Jing Leng[1], Shengye Jin[1] & Wenming Tian[1]

Charge-transfer (CT) states with long transport distances are highly desired for promoting the performance of organic optoelectronic devices in photoconversion and electroluminescence. However, due to the limited lifetime and small diffusivity, only nanoscale CT transport has been observed so far. Herein, taking a binary CT cocrystal (*trans*–1,2-diphenylethylene-1,2,4,5-tetracyanobenzene, named as T_S-T_C) with efficient thermally activated delayed fluorescence (TADF) as a model material, we report the direct observation of long-distance CT exciton transport by using modified time-resolved and photoluminescence-scanned imaging microscopy, which reveals a triplet-assisted CT transport mechanism. We demonstrate that, enabled by the long-lived and high-yield triplet state and efficient TADF, the average transport distance of over 80% of CT excitons in T_S-T_C can be significantly enhanced from intrinsic nanoscale (≤58 nm) to ~11.2 µm. Our findings provide an effective strategy for greatly promoting short-lived CT exciton transport, which is of great significance for optoelectronic material design and device optimization.

Charge-transfer (CT) excitons, composed of bound electron-hole pairs delocalized across the adjacent donor-acceptor (D-A) interface, have been widely observed in organic semiconductor heterojunctions[1–6]. As important intermediates between tightly bound excitons and free carriers, CT excitons, especially their transport features, are central to functions like photoconversion and electroluminescence, making them crucial in various organic optoelectronic devices[7–12]. For example, in bulk-heterojunction organic photovoltaics (OPVs), the mobile CT states will facilitate the migration of CT excitons towards the lower-energy sites along the D-A interface, thereby providing additional opportunities for efficient exciton dissociation into free carriers[13,14]; while in third-generation organic light emitting diodes (OLEDs) with two host and one guest materials[1], the diffusive CT states may promote energy transfer to the diluted luminescent guest, thus improving the exciton harvesting and device performance.

With the rapid advancement of organic optoelectronic devices, the CT exciton transport, determined by their diffusivity and lifetime, has become the focus of both experimental and theoretical investigations[12,14–18]. However, due to the negligible absorption and weakly bound property of CT excitons, both the Förster and Dexter energy transfer (EnT) in D-A blends may exhibit relatively low efficiency, resulting in their small diffusivity[14–16]. On the other side, the presence of Coulomb interaction in CT excitons also leads to their finite lifetimes (often within nanosecond timescale). Therefore, the transport distances of CT excitons are usually confined within tens of nanometers as reported in various D-A blend systems[14,16,19]. In this

---

[1]State Key Laboratory of Chemical Reaction Dynamics, Dalian Institute of Chemical Physics, Chinese Academy of Sciences, Dalian, China. [2]University of Chinese Academy of Sciences, Beijing, China. [3]Instrumental Analysis Center, Dalian University of Technology, Dalian, China. [4]State Key Laboratory of Catalysis, Dalian National Laboratory for Clean Energy, Dalian Institute of Chemical Physics, Chinese Academy of Sciences, Dalian, China.
e-mail: yjxiao@dicp.ac.cn; ljjx@dicp.ac.cn; sjin@dicp.ac.cn; tianwm@dicp.ac.cn

regard, developing an effective strategy for achieving long-distance CT exciton transport is highly desired for the potentially enhanced device performance.

A viable solution involves enhancing the carrier lifetime and/or diffusivity. The triplet excitons usually exhibit long lifetimes due to the spin-forbidden transition, enabling their long-distance diffusions over several micrometers[20–23]. Recently, Huang et al. reported a singlet-mediated triplet transport mechanism utilizing singlet fission, which significantly increases the triplet diffusivity by more than one order of magnitude[24,25]. Inspired by this cooperative singlet-triplet transport, we propose that, by employing the long-lived triplet state, the transport distance of CT excitons might also be significantly promoted. Due to the spatially separated highest occupied (HOMO) and lowest unoccupied molecular orbitals (LUMO), the singlet-triplet (^{1}CT-^{3}CT) exchange energy (ΔE_{ST}) of CT excitons is notably narrowed, which facilitates the reverse intersystem crossing (RISC) process from ^{3}CT to ^{1}CT state and easily leads to the efficient emission of thermally activated delayed fluorescence (TADF)[1,26–28]. The efficient TADF of CT excitons, along with their long-lived ^{3}CT state, enables them to exhibit great potential for achieving long-distance CT exciton transport. To assess the potential of this triplet-assisted CT transport mechanism, a thorough understanding of the interplay between TADF and CT exciton transport is therefore in demand.

To address this issue, we endeavor to integrate the conventional phosphorescence decay recording method based on time-correlated single photon counting (TCSPC) technique with our PL-scanned imaging microscopy to realize the direct observation of CT transport on both nano- and milli-second timescales. On the other hand, CT cocrystals, composed of two or more donor and acceptor monomers, are primarily considered as promising candidates for exploring CT dynamics due to their well-defined structure, low defect density, and intense CT absorption[29–34]. In this work, taking a binary CT cocrystal (*trans*−1,2-diphenylethylene-1,2,4,5-tetracyanobenzene, named as T_S-T_C) with efficient TADF emission as a model material, we successfully observed a long-distance CT exciton transport and revealed a triplet-assisted CT transport mechanism. We demonstrated that, by utilizing a long-lived and high-yield ^{3}CT state, the average transport distance of over 80% of CT excitons in T_S-T_C can be potentially increased by more than two orders of magnitude to ~11.2 µm.

Results and discussion

Optical absorption and emission of T_S-T_C

Ribbon-like T_S-T_C cocrystal with a good phase purity was primarily synthesized following a previously reported solution drop-casting method (Supplementary Fig. 1, Fig. 2 and see Methods for more details)[35,36]. As revealed by the single-crystal X-ray diffraction (SXRD) analyses (details of the refinement data are provided in Supplementary Table 1), T_S-T_C cocrystal exhibits the common mixed-stacking motif with a 1:2 D/A stoichiometry. Each benzene ring of TSB (*trans*-1,2-diphenylethylene) is overlapped by a TCNB (1,2,4,5-tetracyanobenzene) molecule with the measured D-A intermolecular distance of 3.38 Å (Supplementary Fig. 3). The short D-A distance can facilitate the π-electron delocalization from TSB to TCNB, leading to the intermolecular charge-transfer feature of T_S-T_C (Fig. 1a). The absorption edge and the PL emission peak of T_S-T_C are located at ~550 nm and ~570 nm respectively (Fig. 1b), both of which are apparently red-shifted compared with its individual components (Supplementary Fig. 4), demonstrating the notable CT feature of T_S-T_C cocrystal.

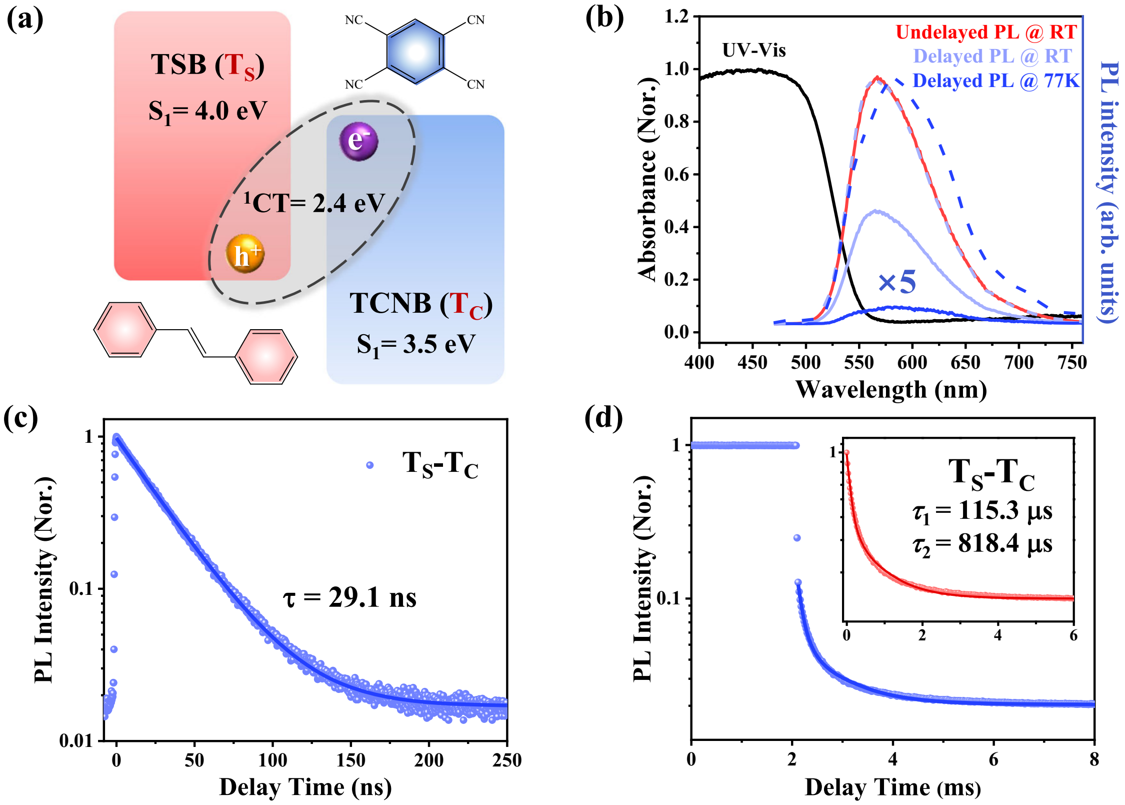

Fig. 1 | Chemical composition and optical properties of T_S-T_C cocrystal. a Energy diagram and chemical structures of binary T_S-T_C cocrystal. **b** Absorption (black), undelayed PL (red) and delayed PL spectra (200 µs after excitation) at room temperature (RT, light blue) and 77 K (blue) of T_S-T_C. The dash lines are the normalized delayed PL spectra at RT (light blue) and 77 K (blue) respectively, for comparison with the undelayed PL spectrum. PL kinetics collected on (**c**) nanosecond timescale and (**d**) millisecond timescale based on normal TCSPC technique and multipulse-excited TCSPC PDR technique, respectively. Insert of (**d**) is a delayed PL kinetics after deducting initial fluorescence interference. Solid lines in (**c**) and (**d**) are exponential fittings of these kinetics.

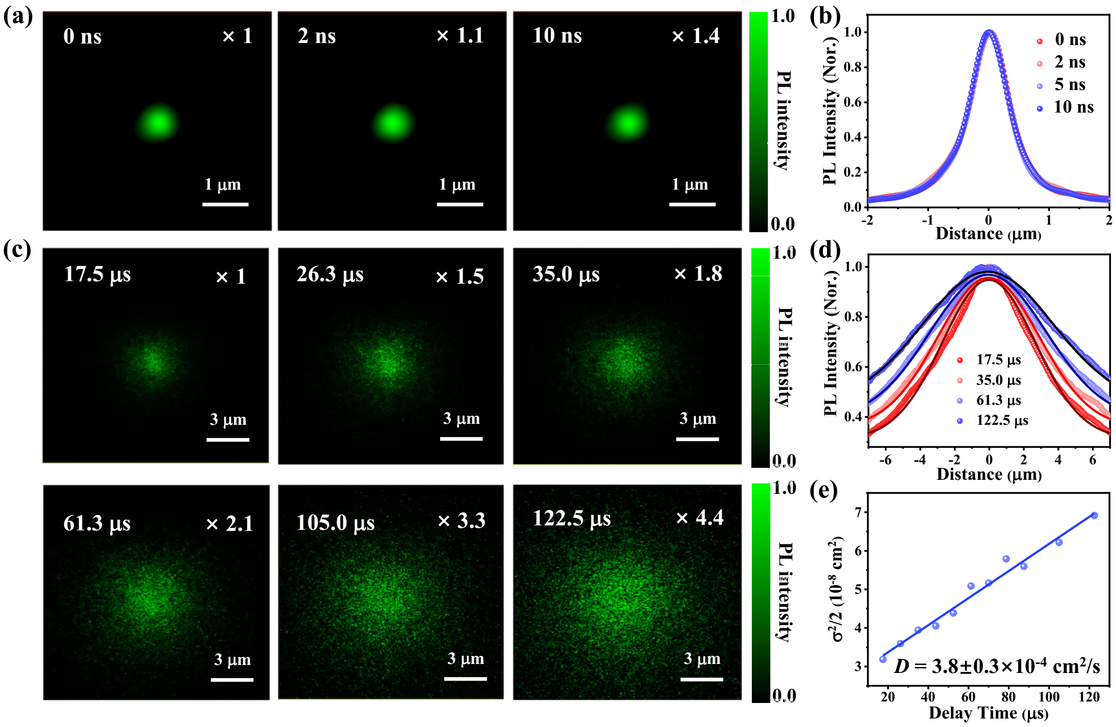

Fig. 2 | Imaging and modeling of CT exciton transport. PL intensity images from (**a**) fluorescence and (**c**) TADF emission in T_S-T_C at different delay times after excitation. Scale bars are 1 μm and 3 μm, respectively. **b** Normalized 1D fluorescence intensity profiles of T_S-T_C extracted from the *x*-axis in (**a**) at different delay times. The fluorescence distributions are almost identical, indicating the ^{1}CT exciton transport distance in T_S-T_C is within the spatial resolution (~58 nm) of ns-scale PL imaging measurements. **d** Normalized 1D TADF intensity profiles extracted from (**c**), along with their Gaussian fittings, showing the spatial broadening of the TADF-related exciton distribution. **e** The determination of TADF-related exciton diffusion coefficient by linearly fitting of the 1D time-dependent Gaussian variances ($\sigma^2(t)$).

To uncover the CT dynamics in T_S-T_C, we then carried out PL kinetic measurements by using TCSPC technique within both nano- and milli-second time windows (Fig. 1c, d). We note that, the ns-scale PL kinetics was collected by the typical TCSPC with a single-pulse excitation, while for PL kinetics on ms scale, a multipulse-excited TCSPC phosphorescence decay recording (PDR) technique was employed to improve the detection sensitivity (Supplementary Fig. 5; for more details see Methods)[37,38]. The fluorescence emission of T_S-T_C exhibits a single exponential decay with a lifetime of ~29.1 ns (Fig. 1c). Besides that, a long-lived PL decay kinetics was also clearly observed on a ms timescale (Fig. 1d), which can be well fitted by a biexponential function, yielding two time constants of 115.3 μs and 818.4 μs (Supplementary Table 2). To avoid fluorescence interference during initial delay times, this data fitting started from the delay time of its second data point (17.5 μs, insert of Fig. 1d).

To clarify the origin of this long-lived emission, we further examined the delayed PL spectra (200 μs after excitation) at room temperature (RT) and 77 K, respectively. The delayed PL emission at RT exhibits an almost identical spectral profile to that of the total (undelayed) PL emission (Fig. 1b), and also similar decay kinetics collected at different wavelength ranges (Supplementary Fig. 6), indicating a typical TADF emission due to the RISC from triplet to singlet state. At 77 K, the delayed TADF emission was found to be prominently quenched and slightly red-shifted, suggesting a promoted phosphorescence emission at lower temperatures. Based on the relative shift between PL and phosphorescence emission peak (~570 nm and ~582 nm, respectively), the singlet-triplet energy gap (ΔE_{ST}) is estimated to be ~45 meV, generally consistent with the previously reported value of ~10 meV[35]. Furthermore, to quantify the proportion of TADF in total PL emission at RT, we directly compared the integrated areas of total and delayed PL spectra (Supplementary Fig. 7a, 7b), from which the TADF weight can be estimated to be ~81%. This value is consistent with the changes in total PL spectra area measured at RT and 77 K (~82%, Supplementary Fig. 7c), indicating an efficient TADF emission.

Visualization and modeling of charge-transfer exciton transport

We next directly imaged the CT transport in T_S-T_C by using time-resolved and PL-scanned imaging microscopy (see Supplementary Fig. 8 and Methods for more details)[39,40]. In brief, the excitation beam was focused to a near diffraction-limited spot (~550 nm in radius, Supplementary Fig. 9a) at a fixed position of T_S-T_C through a 100× air objective (NA = 0.95), and the time-dependent PL intensity images can be obtained by scanning the PL collection spot on T_S-T_C with a pair of galvano-mirrors. For ns-scale PL imaging, the local PL kinetics at any position can be extracted by the TCSPC module. While for PL imaging on the ms scale, the direct visualization of long-distance CT exciton migration was successfully realized using the aforementioned multipulse-excited TCSPC PDR technique.

Figure 2a shows the PL intensity images of T_S-T_C collected at different delay times on a ns timescale. As the PL intensity is proportional to the exciton density, the time evolution of PL intensity distribution can directly reflect the exciton transport process, and the exciton transport in lateral dimension can be further described by a time-dependent two-dimensional (2D) Gaussian function[20,39]:

$$I_{PL}(x,y,t) \propto n(x,y,t) = N\exp\left[-\frac{(x-x_0)^2}{2\sigma_{x,t}^2} - \frac{(y-y_0)^2}{2\sigma_{y,t}^2}\right] \tag{1}$$

where x_0 and y_0 are the central position of Gaussian excitation beam, $\sigma_{x,t}^2$ and $\sigma_{y,t}^2$ are the time-dependent deviation of Gaussian profiles along x and y directions (see Supplementary Note 1 for detailed discussion). Exciton transport will result in the broadening of PL profile (σ) as delay time prolongs. By directly comparing their normalized one-dimensional (1D) profiles of PL intensity (i.e., the cross section of PL image) at different delays, the exciton transport behavior can be more clearly observed and quantitatively determined. As shown in Fig. 2b, there is no obvious broadening of ns-scale PL (fluorescence) intensity profiles, indicating that the intrinsic ^{1}CT transport distance in T_S-T_C is within the spatial resolution of our measurements (~58 nm, Supplementary Note 1).

However, on a millisecond timescale, an apparent spatial expansion of CT exciton distribution can be clearly observed from the TADF intensity images with increased delay times (Fig. 2c), suggesting the notable exciton diffusion away from the initial excitation position. Specially, TADF intensity images after the second data point (t = 17.5 μs) were extracted and compared to circumvent the fluorescence emission during the initial delays. Due to a certain degree of exciton diffusion already occurred at t = 17.5 μs, the initial TADF distribution becomes much broader (~3.5 μm in radius) than the laser excitation spot (~550 nm in radius) (Supplementary Fig. 9). An isotopic exciton diffusion feature can be observed from the TADF imaging as shown in Fig. 2c, which may originate from the comparable distances between neighboring D-A units in T_S-T_C across different directions (Supplementary Fig. 10). According to the solution to diffusion equation, the diffusion coefficient (*D*) of the isotopic CT transport can be directly obtained from a linear fitting of Gaussian variances of 1D PL profiles as a function of delay times (Supplementary Note 1)[24]:

$$D = \frac{\sigma_{x,t}^2 - \sigma_{x,0}^2}{2t} \tag{2}$$

The extracted 1D PL profiles of TADF intensity images can be well described by Gaussian functions (Fig. 2d), and the linear fitting of the time-dependent Gaussian variances yields $D = (3.8 \pm 0.3) \times 10^{-4}$ cm^2/s (Fig. 2e). It should be noted that the excitation intensity for TADF imaging was set to be low enough (i.e., 2.3 μJ/cm^2) to avoid the occurrence of higher-order recombination (Supplementary Fig. 11 and Fig. 12). In addition, we also performed a statistic analysis of the measured *D* values based on the TADF imaging of different T_S-T_C cocrystals (Supplementary Fig. 13). The obtained diffusion coefficients are all in the range of $2.8 \sim 3.8 \times 10^{-4}$ cm^2/s, indicating the high crystal quality of T_S-T_C cocrystals and the reliability of TADF imaging methodology employed in our measurements.

Dynamic mechanism of charge-transfer excitons in T_S-T_C

Although the long-lived PL emission in T_S-T_C has been well confirmed to originate from TADF, the related dynamic mechanism is still confusing considering the biexponential decay feature of TADF (Fig. 1d). Recently, Hu et al. found through theoretical calculations that the two lowest triplet states in T_S-T_C, T_1 (triplet state in TSB) and ^{3}CT, are closely aligned in energy and thermally equilibrated with the ^{1}CT state (Supplementary Fig. 14), and thus proposed a double-channel ISC mechanism for the biexponential TADF decay[35]. However, despite the assumed existence of two feasible ISC/RSIC pathways in T_S-T_C, our findings validate that the TADF kinetics should exhibit the monoexponential decay (see Supplementary Note 2 for detailed derivation), indicating the insufficiency of the double-channel ISC mechanism in explanation of the biexponential TADF decay in T_S-T_C[41].

Based on prior theoretical calculations[35], the relative energy levels and the possible carrier dynamic processes are shown in Fig. 3a. It can be seen that an energy order inversion occurs between T_1 and ^{1}CT states after the photoexcited vibrational relaxation, which actually breaks the dynamic equilibrium between them. Therefore, TADF should be dominated by the RISC process from ^{3}CT to ^{1}CT, and the contribution of T_1-to-^{1}CT channel can be reasonably ignored. The ^{3}CT dominated RISC can be verified by the large magneto-photoluminescence (MPL) effect (~8.6%) observed in T_S-T_C (Supplementary Fig. 15), because Frenkel excitons with strong exchange interaction are generally insensitive to the magnetic field (MPL ~ 1%)[42,43]. Subsequently, we carefully inferred the TADF kinetics and confirmed that the rate constant of TADF (k_{DF}) is determined by both the intrinsic ^{3}CT lifetime (k_3) and the rate constants of ISC (k_1) and RISC (k_2) processes (Supplementary Note 2). To get further insights, delayed PL kinetics at different temperatures were compared in Fig. 3b. The decay profiles at different temperatures are almost identical with that of the phosphorescence emission from ^{3}CT state at 77 K, suggesting a potential k_3-dominant TADF kinetics. Therefore, the CT transport observed via TADF imaging (Fig. 2c) is essentially a portrayal of the diffusion of ^{3}CT excitons. The temperature-insensitive k_3 may be derived from the rigid crystal structure of T_S-T_C as revealed by the comparison of crystallographic data measured at RT and 100 K, respectively (Supplementary Table 1)[44]. Moreover, it should be noted that although the k_3-dominaed TADF kinetics is temperature-insensitive, the TADF process in T_S-T_C still exhibits temperature-dependence as evidenced by the monotonic decrease in PL intensity at lower temperatures (Fig. 3c). In addition, although the ^{1}CT-^{3}CT conversion is normally forbidden in isolated D-A molecules, a T_1-mediated spin-vibronic coupling mechanism could probably enable this conversion in T_S-T_C cocrystal[18,45].

The above discussion theoretically proposes that TADF should always exhibit a monoexponential decay feature. Therefore, we speculate that the measured biexponential TADF kinetics (Fig. 1d) likely originates from the diffusion of ^{3}CT excitons[46]. For examination, we carried out the excitation-radius-dependent TADF kinetic measurements on T_S-T_C (Fig. 3d). As expected, the fast component of TADF kinetics gradually disappeared as the excitation area changed from focused (initial TADF radius ~3.5 μm, Supplementary Fig. 9b) to defocused (initial TADF radius ~6.3 μm, Supplementary Fig. 16) and wide-field (full field of view, ~1000 × 800 μm^2) configuration (Fig. 3d), indicating a progressively eliminated diffusion effect due to the decreased exciton density gradient. According to a 2D exciton diffusion and recombination model (see Supplementary Note 3 for detailed discussion)[46], we further globally fitted the focused and defocused TADF kinetics, yielding the intrinsic ^{3}CT lifetime of 850 μs and ^{3}CT diffusion coefficient of 3.5×10^{-4} cm^2/s (Fig. 3d). Based on the experimentally obtained parameters of k_{PF} (3.44×10^7 s^{-1}), k_{DF} (1.22×10^3 s^{-1}), and the prompt fluorescence and TADF proportions ($\varnothing_{PF} = 0.19$ and $\varnothing_{DF} = 0.81$, see Supplementary Fig. 7), the rate constants of k_0 (^{1}CT recombination), k_1, k_2 and k_3 can be further determined to be 1.0×10^5 s^{-1}, 3.43×10^7 s^{-1}, 4.88×10^3 s^{-1}and 1.21×10^3 s^{-1}, respectively (Supplementary Note 2, illustrated in Fig. 3a). The experimentally determined intrinsic lifetime and diffusion coefficient of ^{3}CT state (826.4 μs and 3.8×10^{-4} cm^2/s shown in Figs. 3a and 2e, respectively) agree well with the theoretically fitted parameters of 850 μs and 3.5×10^{-4} cm^2/s, respectively (Fig. 3d). These agreements not only confirm the fast component of TADF kinetics originating from the ^{3}CT diffusion, but also indicate the high accuracy of TADF imaging measurements based on the multipulse-excited TCSPC PDR technique.

^{3}CT-assisted long-distance ^{1}CT exciton transport

Next, we aim to gain further insight into the CT transport mechanism. Three mechanisms may contribute to the observed spatial diffusion: photon recycling, energy transfer, and charge transfer. The re-absorption effect in photon recycling can be ruled out due to the low self-absorption coefficient of T_S-T_C (Supplementary Fig. 17) and the invariant PL spectra profile at distances far from the excitation spot (Supplementary Fig. 18)[47–49]. Moreover, in typical D-A blends, both Förster and Dexter EnT of CT excitons were argued to be inefficient due to their negligible absorption and weakly bound property, and an asynchronous charge transfer mechanism known as the “inchworm” type transport has been proposed to elucidate the motion of CT excitons[14–16]. While in our T_S-T_C model system, the stronger π-π interaction between D and A molecules (Fig. 1) may facilitate the direct

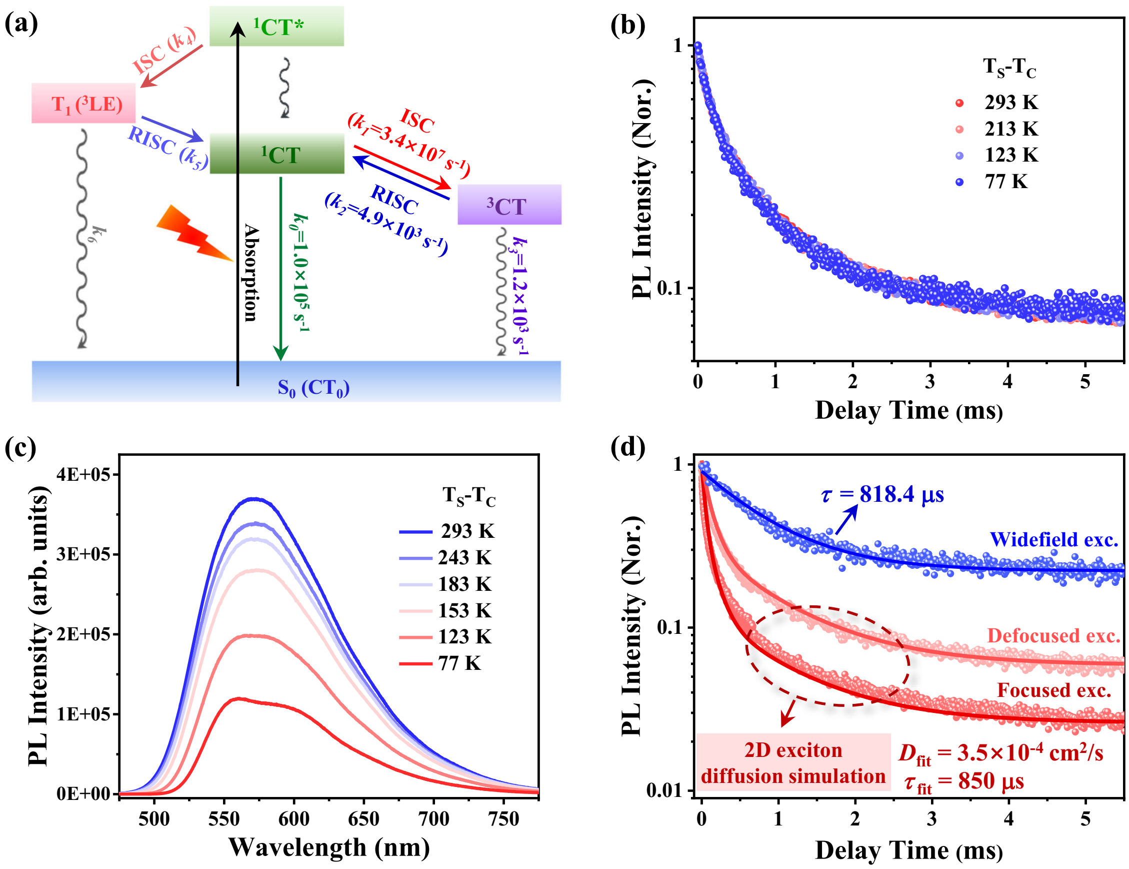

Fig. 3 | Carrier dynamic processes in T_S-T_C cocrystal. **a** Schematic diagram for carrier dynamic processes in T_S-T_C cocrystal. **b** Comparison of delayed PL kinetics collected at different temperatures under 375 nm excitation. These PL kinetics show almost no temperature dependence, indicating the sole TADF emission dominated by the ^{3}CT decay kinetics. **c** Comparison of steady-state PL spectra collected at different temperatures under 375 nm excitation, indicating a typical temperature-dependent TADF emission feature. **d** Comparison of TADF kinetics in T_S-T_C measured under focused (~3.5 μm in initial TADF radius), defocused (~6.3 μm in initial TADF radius) and widefield (in range of ~1000 × 800 μm^2) excitation, showing a gradually eliminated fast decay component due to the reduced impact of ^{3}CT diffusion. Blue solid line is the single-exponential fitting of the widefield kinetics, while the red and dark red ones are the global fits of focused and defocused kinetics in terms of 2D exciton diffusion model described in Supplementary Note 3. The excitation intensity was set to be 2.3 μJ/cm^2 for both focused and defocused excitation, and ~4.5 × 10^{-5} μJ/cm^2 for the widefield excitation.

CT transport in an excitonic form. The tightly bound nature of CT excitons in T_S-T_C can be verified by an excitation-intensity dependent PL intensity measurement (Supplementary Fig. 19), and further corroborated by their exponential decay feature (Fig. 1a)[12]. Therefore, we are prone to retain the Förster and/or Dexter mechanism for demonstrating the CT transport in T_S-T_C.

The ^{3}CT diffusion coefficient of 3.8 × 10^{-4} cm^2/s aligns with the typical triplet diffusion coefficient range (10^{-3}–10^{-4} cm^2/s) observed in other organic semiconductors[21,24], indicating the Dexter EnT mechanism underlies ^{3}CT transport in T_S-T_C. This speculation can be further verified by the PL imaging measurements performed at 243 K. The ^{3}CT diffusion coefficient, determined to be ~5.8 × 10^{-4} cm^2/s at 243 K, is slightly larger than that of 3.8 × 10^{-4} cm^2/s at RT, which confirms the temperature-dependent Dexter-type ^{3}CT transport in T_S-T_C (Supplementary Fig. 20). While for ^{1}CT transport (Fig. 4a), the diffusion coefficient can be roughly estimated to be ≤3.1 × 10^{-4} cm^2/s based on its lifetime (~29.1 ns) and diffusion distance ($L_D \leq 58$ nm, $L_D = 2\sqrt{D\tau}$), indicating a potentially inefficient Förster EnT. Additional PL quenching measurements further yielded an estimated ^{1}CT diffusion coefficient on the order of 10^{-4} cm^2/s (see Supplementary Fig. 21 and Note 4 for detailed discussion)[50], which consists with the maximum ^{1}CT D value of 3.1 × 10^{-4} cm^2/s, and is comparable to the magnitude of ^{3}CT diffusion. Accordingly, we suppose that the ^{1}CT transport in T_S-T_C should also follow the Dexter EnT mechanism rather than the Förster EnT pathway.

In contrast, despite exhibiting a moderate diffusivity (3.8 × 10^{-4} cm^2/s), ^{3}CT excitons in T_S-T_C can realize a remarkable diffusion over ~11.2 μm because of their long lifetimes (826.4 μs). Meanwhile, due to the small ^{1}CT-^{3}CT energy difference in T_S-T_C, the migrative ^{3}CT excitons can regenerate into ^{1}CT excitons through the effective RISC, thereby resulting in an equivalent long-distance ^{1}CT exciton transport assisted by the ^{3}CT state. Based on the above discussion, we proposed a ^{3}CT-assisted long-distance CT exciton transport mechanism as illustrated in Fig. 4b. Despite the inefficient EnT and short lifetime of ^{1}CT excitons limiting their intrinsic diffusion within 58 nm (Fig. 4a), the transport distance can be remarkably promoted beyond two orders of magnitude through the ^{3}CT-assisted pathway, which is facilitated by the efficient TADF and long-lived ^{3}CT state (Fig. 4b). Moreover, based on the previously estimated TADF proportion (Supplementary Fig. 7a), the triplet yield in T_S-T_C was further inferred to be >81% (Supplementary Note 2), which indicates that over 80% of CT excitons in T_S-T_C have an average diffusion distance of over 10 μm with the assistance of ^{3}CT state.

The long-distance CT transport is highly desired for promoting device performance in photoconversion and electroluminescence, but hard to realize because of their small diffusivity and short lifetime in most D-A blend systems[12,14,19,51]. We believe that the proposed triplet-assisted CT transport mechanism here may provide an effective strategy to tackle this challenge. For CT excitons with effective TADF, their triplet states can serve as potential energy

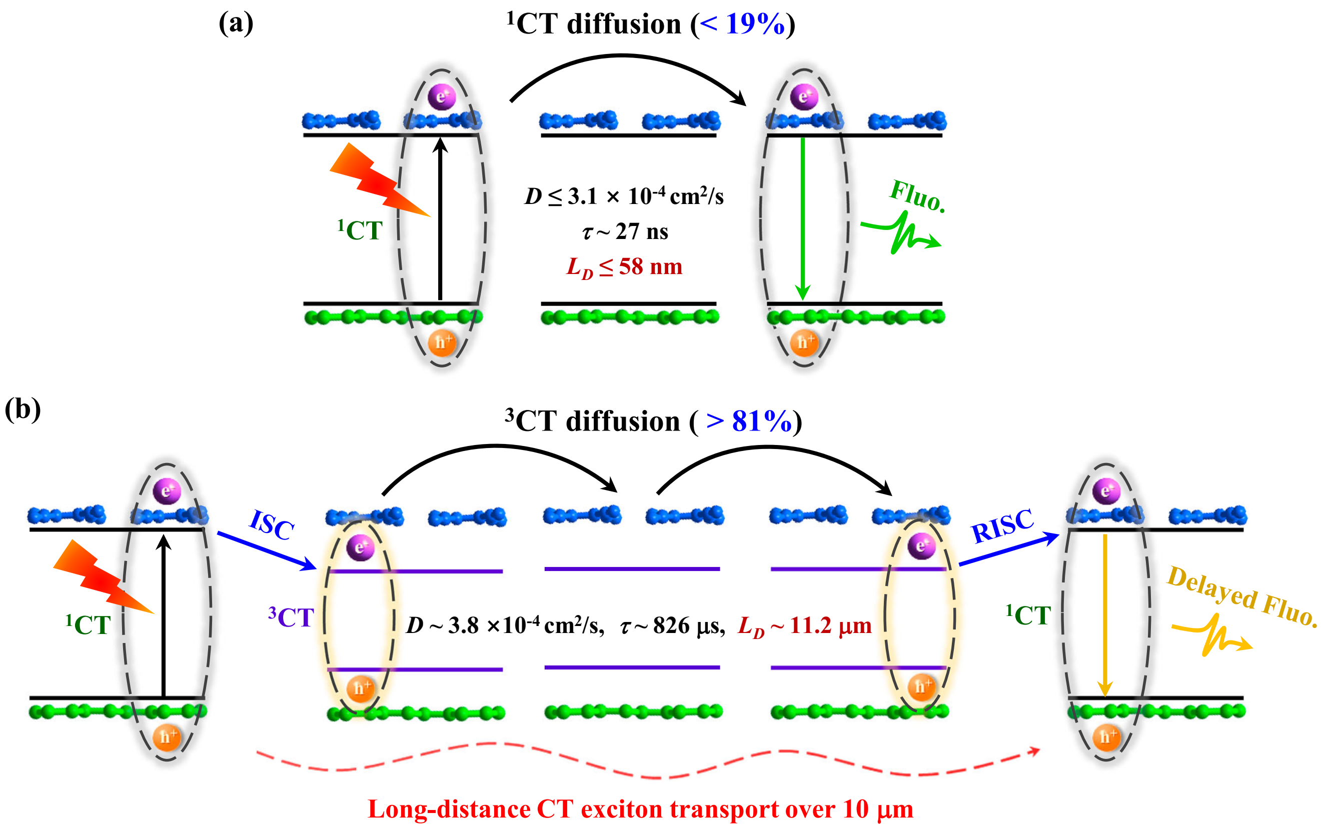
(a)
^{1}CT diffusion (< 19%)
^{1}CT
$D \leq 3.1 \times 10^{-4}$ cm^2/s
$\tau \sim 27$ ns
$L_D \leq 58$ nm
Fluo.
e⁻
h⁺
(b)
^{3}CT diffusion (> 81%)
^{1}CT
ISC
^{3}CT
$D \sim 3.8 \times 10^{-4}$ cm^2/s, $\tau \sim 826$ μs, $L_D \sim 11.2$ μm
RISC
^{1}CT
Delayed Fluo.
Long-distance CT exciton transport over 10 μm

Fig. 4 | CT exciton transport in T_S-T_C. Schematics of (**a**) the intrinsic nanoscale ^{1}CT exciton transport and (**b**) the triplet-assisted micron-scale CT exciton transport.

reservoirs where singlet excitons are quickly "stored" through the ISC process and undergo long-distance diffusion due to the long-lived feature of the triplet state, and then triplet excitons can return to the singlet via rapid RISC. Accordingly, a long-lived and high-yield triplet state combined with efficient TADF is integral to realizing the micron-scale CT transport. To verify the universality of the triplet-assisted CT transport mechanism, an additional TADF cocrystal (T_X-T_C, thioxanthone-1,2,4,5-tetracyanobenzene) was further synthesized[52,53]. Similar triplet-assisted CT transport over 5 μm was observed in this cocrystal (Supplementary Fig. 22), preliminarily confirming the universality of the proposed mechanism for enhancing the singlet diffusion in other TADF materials. The ability to achieve micron-scale CT exciton diffusion has important implications for optoelectronic applications. For instance, it holds great promise for resolving the longstanding contradiction between the nanoscale exciton diffusion lengths and the micron-scale optical absorption depths in OPVs[17,54,55]. Accordingly, detailed investigations into typical TADF film systems are currently in progress and will be presented in future work.

In summary, by coupling the multipulse-excited TCSPC PDR technique with PL-scanned imaging microscopy, we successfully visualized the long-distance CT transport in a binary T_S-T_C cocrystal. The narrowed energy gap between ^{1}CT and ^{3}CT states not only facilitates the TADF emission of T_S-T_C, but also enables an efficient triplet-assisted transport channel. More than 80% of CT excitons can promisingly overcome the intrinsic nanoscale (≤58 nm) transport to achieve the long-distance migration over an average distance of 10 μm. We believe that this triplet-assisted, long-distance CT transport mechanism should also occur in other TADF materials with long-lived triplet states, which exhibits significant implications for improving exciton transport in TADF materials and their further applications in optoelectronics.

Methods

Synthesis of T_S-T_C cocrystal

The T_S-T_C cocrystals were synthesized by a solution self-assembly method. A mixture of TSB (18.0 mg, 0.1 mmol) and TCNB (35.6 mg, 0.2 mmol) was dissolved in 10 ml acetonitrile solvent and directly dropped of the mixed solution onto the substrate. Yellow ribbon-like T_S-T_C cocrystals were obtained after the complete evaporation of solvent.

Material characterizations

X-ray diffraction (XRD) pattern was obtained by using a X'pert Pro X-Ray Diffractometer (PANAlytical, Netherlands) using Cu Kα radiation. A scan rate of 5° min^{-1} was applied in the range of 5–35°. Diffraction intensity data for single crystals of T_S-T_C was collected on a GeminiUltra diffractometer equipped with graphite-monochromatic Mo Kα radiation ($\lambda = 0.71073$ Å). The structure of T_S-T_C was solved by direct methods and refined by full-matrix least-squares techniques based on F^2 using the SHELXS-97 programs[56]. All the non-hydrogen atoms were refined with anisotropic parameters, while hydrogen atoms were placed in calculated positions and refined using a riding model. UV-Vis diffuse reflectance spectra (DRS) were recorded using a UV-Vis spectrophotometer (JASCO V-550) equipped with an integrating sphere, and $BaSO_4$ powder was used as the reference for the baseline correction. Micro-UV–vis absorption spectra were recorded using a UV–Vis–NIR microspectrophotometer (CRAIC Technologies Inc., CRAIC 20/30PV Pro).

PL and delayed PL measurements

The PL imaging and kinetic measurements on nanosecond time scale were performed on a home-built PL-scanned imaging microscopy coupled with a time-correlated single photon counting (TCSPC) module. The setup shown in Supplementary Fig. 8 contains both wide-field (defocused) and focused illumination modules. A 375 nm pulse laser (PDL 800-B, PicoQuant) was focused on the sample through a 100× air objective lens (NA = 0.95, Olympus PLFLN) with the spot radius of ~550 nm. The excitation intensity is adjusted by a neutral density filter and measured with a power meter (PM100D S130VC, Thorlabs, USA). Fixing the excitation spot at a selected position on the sample, the PL emission from the whole sample can be collected by the fast rotation of a pair of galvanometer mirrors. Each scanning image contains 256 × 256 pixels (19 nm/pixel). The PL kinetics was collected by a high-speed detector (HPM-100-50, Hamamatsu, Japan) equipped with a 510 nm long pass filter. The steady-state PL emission spectra were obtained by a monochromator (SpectraPro-HRS-300, Princeton Instruments, USA) coupled with a charge coupled device (CCD) camera (PIXIS 100, Princeton Instruments, USA).

The delayed PL imaging and kinetic measurements were performed on the same setup with an on-off modulated 375 nm pulse laser for excitation. The repetition rate is 50 MHz, and the pixel time (T_{pxl}) is set to be 9 ms with laser-on time (T_{on}) of 3 ms and off time (T_{off}) of 6 ms. For wide-field (defocused) excitation, the excitation laser beam was uncollimated before the 100× air objective lens to form an excitation spot of ~10 μm in diameter. The scanning images of delayed PL contain 256 × 256 pixels (64 nm/pixel). The delayed PL kinetics was collected by a high-speed detector (HPM-100-50, Hamamatsu, Japan) equipped with appropriate band-pass filters. For measurements of temperature-dependent delayed PL kinetics, a 100× air objective lens with NA = 0.6 (Olympus SLMPlan N) was used instead. The delayed PL spectra were measured on a photoluminescence spectrometer (FLS1000, Edinburgh, UK). A 375 nm pulse laser was used for excitation, and the integration time window of the delayed PL spectra was set from 200 μs to 6 ms.

Magneto-photoluminescence (MPL) measurements

All MPL measurements were carried out in the vacuum chamber with a pressure <2.0 torr in a cryostat integrated with an electromagnet (OptiCool, Quantum Design). A 405 nm pulse laser (LDH-IB-405-B, PicoQuant) was used for excitation, and the spectra were acquired by a monochromator (SpectraPro-HRS-300, Princeton Instruments, USA) coupled with a charge coupled device (CCD) camera (PIXIS 100, Princeton Instruments, USA).

Data availability

All raw data generated within the article and the Supplementary Information are available from the Source Data File. Source data are provided with this paper.

References

1. Sarma, M., Chen, L.-M., Chen, Y.-S. & Wong, K.-T. Exciplexes in OLEDs: principles and promises. *Mater. Sci. Eng. R Rep.* **150**, 100689 (2022).
2. Coropceanu, V., Chen, X.-K., Wang, T., Zheng, Z. & Bredas, J.-L. Charge-transfer electronic states in organic solar cells. *Nat. Rev. Mater.* **4**, 689–707 (2019).
3. Dimitriev, O. P. Dynamics of excitons in conjugated molecules and organic semiconductor systems. *Chem. Rev.* **122**, 8487–8593 (2022).
4. Go, E. et al. Spectrally resolved exciton polarizability for understanding charge generation in organic bulk hetero-junction diodes. *J. Am. Chem. Soc.* **146**, 14724–14733 (2024).
5. Ostroverkhova, O. Organic optoelectronic materials: mechanisms and applications. *Chem. Rev.* **116**, 13279–13412 (2016).
6. Hinrichsen, T. F. et al. Long-lived and disorder-free charge transfer states enable endothermic charge separation in efficient non-fullerene organic solar cells. *Nat. Commun.* **11**, 5617 (2020).
7. Gillett, A. J. et al. The role of charge recombination to triplet excitons in organic solar cells. *Nature* **597**, 666–671 (2021).
8. Goushi, K., Yoshida, K., Sato, K. & Adachi, C. Organic light-emitting diodes employing efficient reverse intersystem crossing for triplet-to-singlet state conversion. *Nat. Photonics* **6**, 253–258 (2012).
9. Jungbluth, A. et al. Limiting factors for charge generation in low-offset fullerene-based organic solar cells. *Nat. Commun.* **15**, 5488 (2024).
10. Madhu, M., Ramakrishnan, R., Vijay, V. & Hariharan, M. Free charge carriers in homo-sorted p-stacks of donor-acceptor conjugates. *Chem. Rev.* **121**, 8234–8284 (2021).
11. Mikhnenko, O. V., Blom, P. W. M. & Thuc-Quyen, N. Exciton diffusion in organic semiconductors. *Energy Environ. Sci.* **8**, 1867–1888 (2015).
12. Zhu, T. et al. Highly mobile charge-transfer excitons in two-dimensional WS_2/tetracene heterostructures. *Sci. Adv.* **4**, eaao3104 (2018).
13. Sajjad, M. T., Ruseckas, A. & Samuel, I. D. W. Perspective enhancing exciton diffusion length provides new opportunities for organic photovoltaics. *Matter* **3**, 341–354 (2020).
14. Deotare, P. B. et al. Nanoscale transport of charge-transfer states in organic donor-acceptor blends. *Nat. Mater.* **14**, 1130–1134 (2015).
15. Lee, C. K., Shi, L. & Willard, A. P. A model of charge-transfer excitons: diffusion, spin dynamics, and magnetic field effects. *J. Phys. Chem. Lett.* **7**, 2246–2251 (2016).
16. Kim, H.-B. & Kim, J.-J. Diffusion mechanism of exciplexes in organic optoelectronics. *Phys. Rev. Appl.* **13**, 024006 (2020).
17. Wang, R. et al. Charge separation from an intra-moiety intermediate state in the high-performance PM6:Y6 organic photovoltaic blend. *J. Am. Chem. Soc.* **142**, 12751–12759 (2020).
18. Williams, M. L., Schlesinger, I., Jacobberger, R. M. & Wasielewski, M. R. Mechanism of ultrafast triplet exciton formation in single cocrystals of π-stacked electron donors and acceptors. *J. Am. Chem. Soc.* **144**, 18607–18618 (2022).
19. Zhang, T., Concannon, N. M. & Holmes, R. J. Migration of charge-transfer states at organic semiconductor heterojunctions. *ACS Appl. Mater. Interfaces* **12**, 31677–31686 (2020).
20. Akselrod, G. M. et al. Visualization of exciton transport in ordered and disordered molecular solids. *Nat. Commun.* **5**, 3646 (2014).
21. Irkhin, P. & Biaggio, I. Direct imaging of anisotropic exciton diffusion and triplet diffusion length in rubrene single crystals. *Phys. Rev. Lett.* **107**, 017402 (2011).
22. Luppi, B. T., Majak, D., Gupta, M., Rivard, E. & Shankar, K. Triplet excitons: improving exciton diffusion length for enhanced organic photovoltaics. *J. Mater. Chem. A* **7**, 2445–2463 (2019).
23. Najafov, H., Lee, B., Zhou, Q., Feldman, L. C. & Podzorov, V. Observation of long-range exciton diffusion in highly ordered organic semiconductors. *Nat. Mater.* **9**, 938–943 (2010).
24. Wan, Y. et al. Cooperative singlet and triplet exciton transport in tetracene crystals visualized by ultrafast microscopy. *Nat. Chem.* **7**, 785–792 (2015).
25. Zhu, T., Wan, Y., Guo, Z., Johnson, J. & Huang, L. Two birds with one stone: tailoring singlet fission for both triplet yield and exciton diffusion length. *Adv. Mater.* **28**, 7539–7547 (2016).
26. Cui, L.-S. et al. Fast spin-flip enables efficient and stable organic electroluminescence from charge-transfer states. *Nat. Photonics* **14**, 636–642 (2020).
27. Han, C. et al. Ladder-like energy-relaying exciplex enables 100% internal quantum efficiency of white TADF-based diodes in a single emissive layer. *Nat. Commun.* **12**, 3640 (2021).
28. Uoyama, H., Goushi, K., Shizu, K., Nomura, H. & Adachi, C. Highly efficient organic light-emitting diodes from delayed fluorescence. *Nature* **492**, 234–238 (2012).
29. Sun, L. et al. Creating organic functional materials beyond chemical bond synthesis by organic cocrystal engineering. *J. Am. Chem. Soc.* **143**, 19243–19256 (2021).

30. Yu, Y. et al. Customizable organic charge-transfer cocrystals for the dual-mode optoelectronics in the NIR (II) window. *J. Am. Chem. Soc.* **146**, 11845–11854 (2024).
31. Wang, X. et al. Elimination of charge accumulation by a self-assembled cocrystal interlayer for efficient and stable perovskite solar cells. *Energy Environ. Sci.* **17**, 569–579 (2024).
32. Sun, L., Wang, Y., Yang, F., Zhang, X. & Hu, W. Cocrystal engineering: a collaborative strategy toward functional materials. *Adv. Mater.* **31**, 1902328 (2019).
33. Ye, H. Q. et al. Molecular-barrier-enhanced aromatic fluorophores in cocrystals with unity quantum efficiency. *Angew. Chem. Int. Ed.* **57**, 1928–1932 (2018).
34. Wang, X. et al. Recent advances of organic cocrystals in emerging cutting-edge properties and applications. *Angew. Chem. Int. Ed.* **63**, e202416181 (2024).
35. Sun, L. et al. Thermally activated delayed fluorescence in an organic cocrystal: narrowing the singlet-triplet energy gap via charge transfer. *Angew. Chem. Int. Ed.* **58**, 11311–11316 (2019).
36. Xiao, Y. et al. Ternary cocrystal with long-lived charge-transfer state for efficient light conversion applications. *Adv. Optical Mater.* **12**, 2400747 (2024).
37. Howard, S. S., Straub, A., Horton, N. G., Kobat, D. & Xu, C. Frequency-multiplexed in vivo multiphoton phosphorescence lifetime microscopy. *Nat. Photonics* **7**, 33–37 (2013).
38. Baggaley, E. et al. Long-lived metal complexes open up microsecond lifetime imaging microscopy under multiphoton excitation: from FLIM to PLIM and beyond. *Chem. Sci.* **5**, 879–886 (2014).
39. Sun, Q. et al. Long-range exciton transport in perovskite-metal organic framework solid composites. *J. Phys. Chem. Lett.* **11**, 9045–9050 (2020).
40. Zhao, C. et al. Trap-enabled long-distance carrier transport in perovskite quantum wells. *J. Am. Chem. Soc.* **142**, 15091–15097 (2020).
41. Kim, H. S., Lee, S. H., Yoo, S. & Adachi, C. Understanding of complex spin up-conversion processes in charge-transfer-type organic molecules. *Nat. Commun.* **15**, 2267 (2024).
42. Wang, H. et al. Giant magneto-photoluminescence at ultralow field in organic microcrystal arrays for on-chip optical magnetometer. *Nat. Commun.* **15**, 3995 (2024).
43. Xu, H., Wang, M., Yu, Z. G., Wang, K. & Hu, B. Magnetic field effects on excited states, charge transport, and electrical polarization in organic semiconductors in spin and orbital regimes. *Adv. Phys.* **68**, 49–121 (2019).
44. Zhao, W., He, Z. & Tang, B. Z. Room-temperature phosphorescence from organic aggregates. *Nat. Rev. Mater.* **5**, 869–885 (2020).
45. Etherington, M. K., Gibson, J., Higginbotham, H. F., Penfold, T. J. & Monkman, A. P. Revealing the spin-vibronic coupling mechanism of thermally activated delayed fluorescence. *Nat. Commun.* **7**, 13680 (2016).
46. Zhao, C. Y. et al. Diffusion-correlated local photoluminescence kinetics in $CH_3NH_3PbI_3$ perovskite single-crystalline particles. *Sci. Bull.* **61**, 665–669 (2016).
47. Giovanni, D. et al. Origins of the long-range exciton diffusion in perovskite nanocrystal films: photon recycling vs exciton hopping. *Light Sci. Appl.* **10**, 2 (2021).
48. Yablonovitch, E. & Cody, G. D. Intensity enhancement in textured optical sheets for solar cells. *IEEE Trans. Electron Devices* **29**, 300–305 (1982).
49. Diab, H. et al. Impact of reabsorption on the emission spectra and recombination dynamics of hybrid perovskite single crystals. *J. Phys. Chem. Lett.* **8**, 2977–2983 (2017).
50. Leng, J., Liu, J. X., Zhang, J. & Jin, S. Y. Decoupling interfacial charge transfer from bulk diffusion unravels its intrinsic role for efficient charge extraction in perovskite solar cells. *J. Phys. Chem. Lett.* **7**, 5056–5061 (2016).
51. Zhang, J., Zhu, X., Wang, M. & Hu, B. Establishing charge-transfer excitons in 2D perovskite heterostructures. *Nat. Commun.* **11**, 2618 (2020).
52. Wen, T. et al. Transforming thermally activated delayed fluorescence to room-temperature phosphorescence through modulation of the donor in charge-transfer cocrystals. *J. Phys. Chem. Lett.* **15**, 2690–2696 (2024).
53. Aizawa, N. et al. Delayed fluorescence from inverted singlet and triplet excited states. *Nature* **609**, 502–506 (2022).
54. Li, Q. et al. Long-range charge separation enabled by intramoiety delocalized excitations in copolymer donors in organic photovoltaic blends. *J. Phys. Chem. Lett.* **14**, 7498–7506 (2023).
55. Chandrabose, S. et al. High exciton diffusion coefficients in fused-ring electron acceptor films. *J. Am. Chem. Soc.* **141**, 6922–6929 (2019).
56. Feldblyum, J. I., Keenan, E. A., Matzger, A. J. & Maldonado, S. Photoresponse characteristics of archetypal metal-organic frameworks. *J. Phys. Chem. C* **116**, 3112–3121 (2012).

Acknowledgements

We acknowledge support from the CAS projects for Young Scientists in Basic Research (YSBR-007 to S.J.), the Strategic Priority Research Program of the Chinese Academy of Sciences (XDB0970302 to W.T.), the National Natural Science Foundation of China (No. 22233005 to S.J., 22439001 to J.L., 22303105 to Y.X., 22122307 to W.T.), the Natural Science Foundation of Liaoning (2024JH3/50100010 to W.T.), the Liaoning Revitalization Talents Program (XLYC2203043 to W.T.), the Dalian Science and Technology Innovation Fund (2024RJ006 to W.T., 2024RQ021 to Y.X.) and the DICP funding (DICP I202206 to J.L., I202315 to W.T.). We thank Dr. Yuan CHENG from the Instrumentation and Service Center for Molecular Sciences at Westlake University for the assistance in micro-UV-vis absorption spectra measurements.

Author contributions

W.T., S.J., J.L. and Y.X. conceived the project, Y.X. performed the sample preparation and characterization measurements, X.Y. designed the imaging technique, Y.X. performed the experiment and data analysis with the assistance X.Y., J.B. and M.Z., R.C. performed delayed PL measurement, X.L. contributed to the data analysis. The manuscript was drafted by Y.X. and revised by J.L., S.J. and W.T. All the authors discussed the results and contributed to the manuscript.

Competing interests

The authors declare no competing interests.

Additional information

Supplementary information The online version contains supplementary material available at https://doi.org/10.1038/s41467-025-63388-0.

Correspondence and requests for materials should be addressed to Yejun Xiao, Jing Leng, Shengye Jin or Wenming Tian.

Peer review information *Nature Communications* thanks the anonymous, reviewer(s) for their contribution to the peer review of this work. A peer review file is available.

Reprints and permissions information is available at http://www.nature.com/reprints

Publisher's note Springer Nature remains neutral with regard to jurisdictional claims in published maps and institutional affiliations.

Open Access This article is licensed under a Creative Commons Attribution 4.0 International License, which permits use, sharing, adaptation, distribution and reproduction in any medium or format, as long as you give appropriate credit to the original author(s) and the source, provide a link to the Creative Commons licence, and indicate if changes were made. The images or other third party material in this article are included in the article's Creative Commons licence, unless indicated otherwise in a credit line to the material. If material is not included in the article's Creative Commons licence and your intended use is not permitted by statutory regulation or exceeds the permitted use, you will need to obtain permission directly from the copyright holder. To view a copy of this licence, visit http://creativecommons.org/licenses/by/4.0/.

© The Author(s) 2025